α-Actinin links extracellular matrix rigidity-sensing contractile units with periodic cell-edge retractions

Giovanni Meacci[a,b,†,*], Haguy Wolfenson[a,†,*], Shuaimin Liu[c], Matthew R. Stachowiak[b], Thomas Iskratsch[a,d], Anurag Mathur[c], Saba Ghassemi[c], Nils Gauthier[a,e], Erdem Tabdanov[f], James Lohner[a], Alexander Gondarenko[c], Ashok C. Chander[a], Pere Roca-Cusachs[a,g], Ben O'Shaughnessy[b], James Hone[c], and Michael P. Sheetz[a,e,*]

[a]Department of Biological Sciences, [b]Department of Chemical Engineering, [c]Department of Mechanical Engineering, and [f]Department of Biomedical Engineering, Columbia University, New York, NY 10027; [d]Randall Division of Cell and Molecular Biophysics, King's College London, London SE1 1UL, UK; [e]Mechanobiology Institute, National University of Singapore, Singapore, 117411; [g]Institute for Bioengineering of Catalonia and University of Barcelona, 08028 Barcelona, Spain

ABSTRACT **During spreading and migration, the leading edges of cells undergo periodic protrusion–retraction cycles. The functional purpose of these cycles is unclear. Here, using submicrometer polydimethylsiloxane pillars as substrates for cell spreading, we show that periodic edge retractions coincide with peak forces produced by local contractile units (CUs) that assemble and disassemble along the cell edge to test matrix rigidity. We find that, whereas actin rearward flow produces a relatively constant force inward, the peak of local contractile forces by CUs scales with rigidity. The cytoskeletal protein α-actinin is shared between these two force-producing systems. It initially localizes to the CUs and subsequently moves inward with the actin flow. Knockdown of α-actinin causes aberrant rigidity sensing, loss of CUs, loss of protrusion–retraction cycles, and, surprisingly, enables the cells to proliferate on soft matrices. We present a model based on these results in which local CUs drive rigidity sensing and adhesion formation.**

Monitoring Editor
David G. Drubin
University of California, Berkeley

Received: Feb 17, 2016
Revised: Apr 18, 2016
Accepted: Apr 20, 2016

INTRODUCTION

Integrin-mediated cell-matrix adhesions have long been a subject of interest in cell biology because of the critical effects that the extracellular matrix (ECM) has on cells (Lu *et al.*, 2012; Watt and Huck, 2013; Wolfenson *et al.*, 2013; Humphrey *et al.*, 2014; Iskratsch *et al.*, 2014). Specifically, adhesions play an important role in stabilizing the leading edges of migrating mesenchymal and epithelial cells, thus guiding the directionality of migration (Petrie *et al.*, 2009; Parsons *et al.*, 2010). The dynamic behavior of cell edges during spreading and migration is governed by periodic cycles of protrusion and retraction that are driven by actomyosin-based forces (Giannone *et al.*, 2004, 2007; Dobereiner *et al.*, 2006; Gupton and Waterman-Storer, 2006). One important feature of these cycles is that they require a stiff substrate (e.g., glass); when a cell is plated on a relatively soft substrate (e.g., a 10 kPa gel), the cycles are not observed, and instead there is global ruffling of the cell edge (Giannone *et al.*, 2004). This occurs because adhesion strength is regulated by and proportional to the rigidity of the ECM, and the cell edge is not stabilized on soft matrices (Giannone *et al.*, 2004). This raises the question of how actomyosin forces control rigidity sensing and adhesion strength.

Initial adhesions are assembled at the cell edge as it moves forward and the integrins bind to the ECM through their extracellular domains (Choi *et al.*, 2008; Wolfenson *et al.*, 2013). We recently

This article was published online ahead of print in MBoC in Press (http://www.molbiolcell.org/cgi/doi/10.1091/mbc.E16-02-0107) on April 27, 2016.

†These authors contributed equally to this work.

*Address correspondence to: Giovanni Meacci (giovannimeacci@gmail.com), Haguy Wolfenson (hw2385@columbia.edu), or Michael P. Sheetz (ms2001@columbia.edu).

Abbreviations used: CUs, contractile units; DIC, differential interference contrast; ECM, extracellular matrix; FN, fibronectin; GFP, green fluorescent protein; KD, knockdown; MEF, mouse embryonic fibroblast; PDMS, polydimethylsiloxane; p-MLC, phosphorylated myosin light chain; PMMA, poly(methyl methacrylate); RT, room temperature; shRNA, short hairpin RNA; TIRF, total internal reflection fluorescence.

showed, using submicrometer pillars as substrates for cell spreading, that sarcomere-like contractile units (CUs) in a band of 2–3 μm from the cell edge apply short-term contractions to neighboring nascent adhesions for rigidity sensing (Ghassemi *et al.*, 2012; Wolfenson *et al.*, 2016). This involves bipolar myosin minifilaments that operate on actin filaments (Wolfenson *et al.*, 2016), which are anchored to the integrins through adapter proteins. The local contractions result in normal adhesion development on pillars (Ghassemi *et al.*, 2012), and concomitantly the constant flow of actin from the cell edge toward the nucleus applies inward pulling forces to the adhesions in what has been described as the "integrin clutch model" (Chan and Odde, 2008; Chen *et al.*, 2012; Elosegui-Artola *et al.*, 2014). These two sets of forces are presumably driven by two actomyosin-based networks, lamellar and lamellipodial (Giannone *et al.*, 2007; Xu *et al.*, 2012), which are involved in the protrusion–retraction cycles of the cell edge (Giannone *et al.*, 2007). If and how these cycles are linked (physically and/or mechanistically) to the rigidity-sensing process has not been clear.

In this study, we addressed these questions by analyzing mouse embryonic fibroblasts (MEFs) spreading on fibronectin (FN)-coated glass and 0.5-μm-diameter polydimethylsiloxane (PDMS) pillars. We detected a remarkable correspondence between cell-edge retractions and the peak in force production by CUs. We found that the adhesion and cytoskeletal protein α-actinin provided the link between local CU forces and global actin-flow forces. Depletion of α-actinin resulted in a severe rigidity-sensing defect that allowed the cell to grow on soft matrices, whereas normal cells could not.

RESULTS

Mapping the pattern of cellular forces during cell spreading on pillar arrays

Periodic protrusion–retraction cycles of the cell edge were characterized in a series of studies of early cell spreading in mammalian fibroblasts (Dobereiner *et al.*, 2004, 2006; Giannone *et al.*, 2004, 2007; Dubin-Thaler *et al.*, 2008; Machacek *et al.*, 2009; Gauthier *et al.*, 2011). Because of their regularity and reproducibility, analysis of the protrusion–retraction cycles could provide insight into the mechanisms of motility and mechanosensitivity. However, despite considerable biological, biochemical, and modeling work devoted to understanding the mechanical aspects of this dynamic behavior (Ladoux and Nicolas, 2012; Ryan *et al.*, 2012), the functional purpose of these cycles has not been clear. The above-mentioned studies showed that fibroblast spreading occurred in several stages: initial attachment (P0 stage), rapid increase in contact area (P1), and slower contractile spreading (P2) during which the protrusion–retraction cycles were observed (Dobereiner *et al.*, 2004; Supplemental Figure S1A). However, in these studies, the local forces at the cell edge could not be measured on the stiff continuous substrates used (Giannone *et al.*, 2004; Dubin-Thaler *et al.*, 2008). Thus, to study whether there was a temporal correlation between protrusion–retraction cycles of the cell edge and the generation of force by CUs, we recorded time-lapse bright-field videos at a frame rate of 1 Hz of the spreading process of MEFs on PDMS pillars with 0.5 μm diameter and 1.1 μm height (Supplemental Figure S1B; pillar-bending stiffness = 13.9 pN/nm). On this substrate, the three characteristic spreading phases, P0, P1, and P2, were of similar duration as on flat substrates, and the duration of the protrusion–retraction cycles (observed by differential interference contrast [DIC] microscopy during P2) was 32 ± 10 s (mean ± SD), similar to the value on flat substrates, 23 ± 10 s (Supplemental Figure S1, C and D, and Supplemental Videos S1 and S2; see also Giannone *et al.*, 2004). Thus we concluded that cell behavior on these pillars closely mimicked that on continuous surfaces (see also Ghassemi *et al.*, 2012).

Analysis of pillar movements during the slower spreading phase, P2, showed that the pillars nearest to the leading edge moved inward during a single protrusion–retraction cycle (Figure 1A). These inward displacements (in red at the edge of the cell in Figure 1A) were synchronous with outward displacements of pillars 2–3 μm back from the edge (in green near the edge of the cell in Figure 1A; see also Supplemental Video S3). Control experiments on ultrastiff pillars showed no such correlation, ruling out possible optical artifacts (Figure 1D, Supplemental Figure S1, E and F, and Supplemental Video S4). In nonisotropically spreading cells, the displacement pattern was in general more irregular, with displaced pillars surrounded by nondisplaced pillars, and significant components of the displacement vectors were in multiple directions; however, in isotropically spreading cells with regular protrusion–retraction cycles, the pillar contractions were synchronous over ~10 μm portions of the cell edge, as in the example shown in Figure 1A. Further inward, between the pillar-displacement region at the edge and the nuclear region, pillars showed no significant displacements (Figure 1A). In the nuclear region itself, pillar displacements were significant but randomly directed (Figure 1A).

CUs and actin flow generate forces whose relative contributions depend on matrix stiffness

To further characterize the contractile forces produced by the CUs, we analyzed the direction and coordination of the inward and outward pillar displacements near the leading edge during periodic protrusion–retraction cycles on 13.9 pN/nm pillars. Pillars were first displaced inward near the cell edge, and subsequently displaced outward when they were 2–3 μm behind the edge (Figure 1B and Supplemental Figure S2, A and B). The peak inward displacements, 60 ± 18 nm (all maximal displacements reported here are mean ± SD), were larger than the peak outward displacements, 35 ± 14 nm (Figure 1C). This pattern was not observed on ultrastiff pillars (Figure 1D), and the maximal displacements were random and significantly smaller (Figure 1, E and F). The simultaneous displacements of contractile pillar pairs also indicated that an inward displacement was superimposed on the antiparallel contractile displacement (Supplemental Figure S3, A and B). Looking at the complete CU, a net inward displacement, $\Delta d_{\perp} = 25 \pm 47$ nm, was detected (Supplemental Figure S3C). This observation was in line with the predicted independence of local contractile forces and actin-flow forces (Ghassemi *et al.*, 2012). We calculated that an average inward displacement of ~12.5 nm per pillar was added to an average contractile displacement of ~47.5 nm (47.5+12.5 = 60 nm and 47.5–12.5 = 35 nm for inward and outward displacements, respectively). Thus the local CUs generated on average 3.8-fold greater force per pillar than did the rearward actin flow during cell spreading on these pillars (47.5/12.5 = 3.8). When stiffer pillars were used (43.6 pN/nm), the inward and outward movements were similar at 43 ± 8 and 41 ± 7 nm for the inward and outward moving pillars, respectively (Figure 1G; n = 28 pillars, 3 cells). This indicated that with increased stiffness, the actin flow–based forces had very low contribution to the pillar movements. Also, since the maximal displacements on the stiffer pillars were similar to the 47.5 nm value, this indicated that the contraction stress scaled linearly with substrate rigidity. At the other extreme, when very soft pillars were used (0.8 pN/nm), CUs were very rarely detected, and the pillars were almost exclusively displaced inward by the actin flow (Figure 1G), typically to distances much larger than 47.5 nm (due to optical aberrations originating from the large pillar displacements, the actual

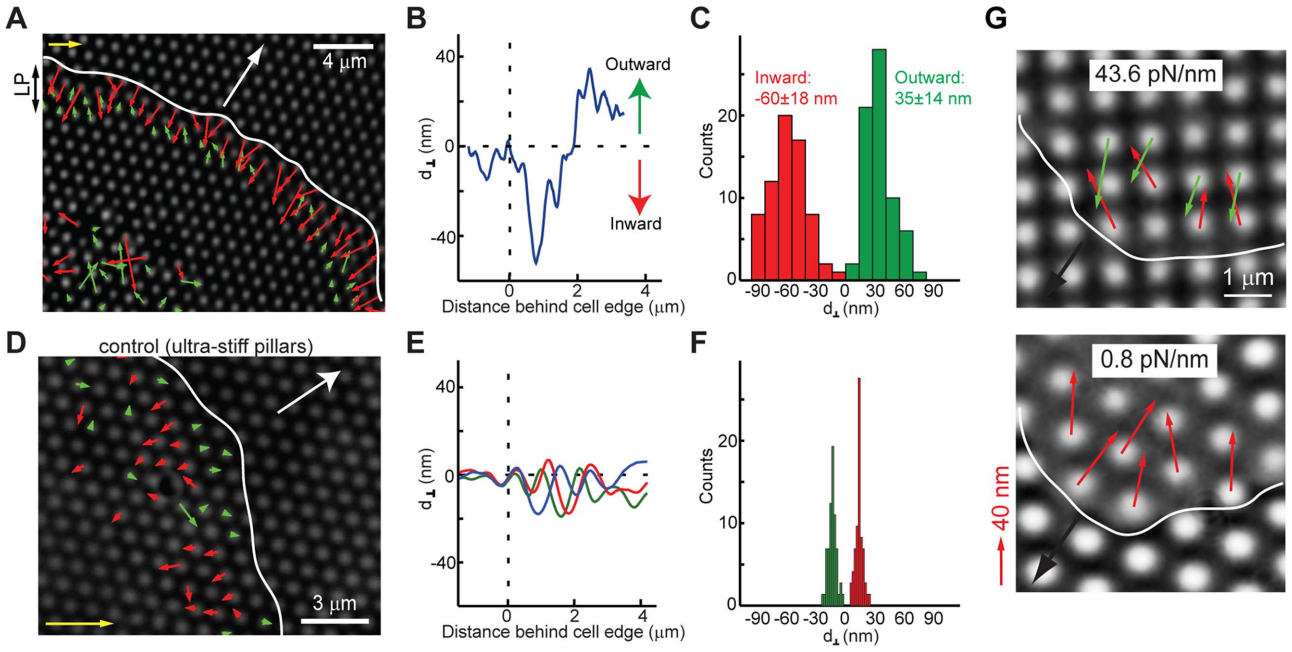

FIGURE 1: Local contractions of the matrix under the cell edge during cell spreading. (A) Typical map of pillar deflections under an isotropically spreading MEF 20 min after plating showing periodic protrusion–retractions. Local contractions involve inward deflections at the leading edge (red arrows) and outward deflections 2–3 μm behind (green arrows). Displacements are shown for pillars that were outside the cell at $t = 0$ s and that had displacements at least fivefold (red arrows) and twofold (green arrows) greater than the average noise (6 nm). Additionally, arrows in and around the nuclear region that were inside the cell at $t = 0$ s are displayed to illustrate the randomly directed displacements under the cell nucleus and the presence of a region between the leading edge and the nuclear region with no significant displacements. White arrow: direction of leading edge extension. Yellow arrow at the top corresponds to 60 nm displacement. (B) Representative trace of a single pillar deflection (stiffness = 13.9 pN/nm) in the direction of the cell motion as a function of distance behind the cell's leading edge. Because displacements were primarily in the direction perpendicular to the cell edge, only the component of the displacement in this direction, $d_\perp$, was plotted. (C) Histograms of maximum outward (green) and inward (red) displacements of pillars with respect to the direction of the cell motion. Differences between inward and outward displacements were significant ($n = 68$ pillars, $p < 0.001$, Mann-Whitney rank-sum test). (D–F) Control experiment on ultrastiff pillars (690 pN/nm): (D) map of pillar deflections under an isotropically spreading cell 20 min after plating. White arrow: direction of leading edge extension. Yellow arrow at the bottom corresponds to 60 nm displacement; (E) three representative traces of single-pillar deflection in the direction of cell motion, $d_\perp$, as a function of distance behind the cell's leading edge; (F) histograms of maximum outward (green) and inward (red) displacements of pillars with respect to the direction of the cell motion for ultrastiff pillars ($n = 52$ pillars from 3 cells). Maximum outward: 9 ± 4 nm; maximum inward: -17 ± 4 nm. (G) Examples of pillar-displacement vectors on stiff (43.6 pN/nm) and ultrasoft (0.8 pN/Nm) pillars.

distances could not be accurately measured, but they were typically larger than 100 nm). This indicated that the force applied to the pillar by the rearward flow were weakly, or not at all, dependent on stiffness, in agreement with our previous results on larger-diameter pillars (see Figure 4, D and E, in Ghassemi *et al.*, 2012).

α-Actinin concentrates in active cell edges and displays a pattern that corresponds to CUs

To test whether there was a correlation between CU-generated forces and periodic edge retractions, we performed temporal analysis of pillar displacements with respect to cell-edge movement. Using the 13.9 pN/nm pillars (on which both CU- and actin flow–based forces could be observed), we found a remarkable correspondence of the maximal displacement of the pillars with the retraction of the cell edge (Figure 2A), indicating that both processes were physically connected. Because α-actinin was involved in both contractile unit formation (Wolfenson *et al.*, 2016) and periodic cell-edge retractions (Giannone *et al.*, 2004, 2007), we postulated that the same complexes might be involved in both processes. Therefore we sought to compare the contraction patterns at the cell edge to the spatial distribution of α-actinin. We first performed time-lapse imaging of the spreading process of green fluorescent protein (GFP)-α-actinin–expressing cells (Figure 2 and Supplemental Video S5). During the P0 phase of spreading (up to ~2 min after the cells were plated), α-actinin was approximately evenly distributed throughout the cell. On the transition to P1 phase, during which there was rapid growth in cell area, α-actinin gradually appeared as a ring around the edge. When the cell transitioned to the contractile phase of spreading (P2), this ring broke, and a differential distribution of α-actinin was observed (Figure 2B). Importantly, at this stage, regular protrusion–retraction cycles only occurred at locations where α-actinin was localized in a band with a width of ~2 μm perpendicular to the leading edge. In neighboring regions with a narrower distribution of α-actinin (or no α-actinin), there were no periodic retractions (in such regions where α-actinin distribution was narrow, the cycles typically dissipated rapidly; Figure 2C and Supplemental Video S5). Line-scan analysis of these wide α-actinin bands in sequential total internal reflection fluorescence (TIRF) images showed that they typically contained two distinct peaks in α-actinin intensity (Figure 2D), which we previously identified as characteristic of the

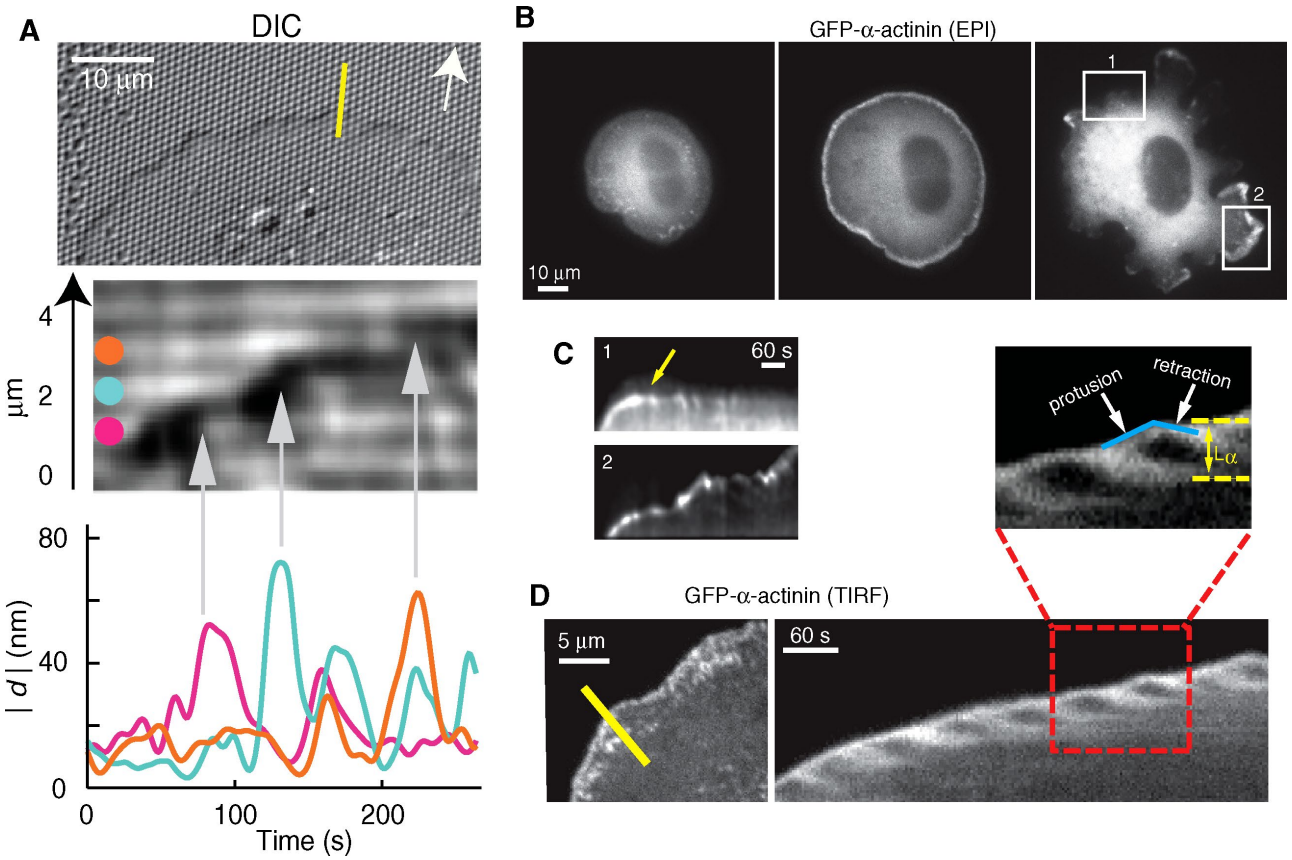

FIGURE 2: α-Actinin localization correlates with protrusion–retraction cycles of the cell edge. (A) Pillar displacement correlates with periodic leading-edge retractions. Top, DIC image of an MEF spreading on PDMS pillars coated with FN (10 µg/ml). White arrow, cell spreading direction. Middle, kymograph from the pillar row indicated in yellow in the DIC image. White horizontal streaks are the pillars; the black streak is the cell's leading edge. Arrows indicate the pillar centers at the times the peaks reach their maximum. Bottom, displacement as a function of time for three pillars in the kymograph, indicated by dots with the same color as the corresponding displacement line. (B) Images from a video taken by epifluorescence microscopy of a GFP-α-actinin–expressing cell spreading on FN-coated glass (10 µg/ml). (C) Top, kymograph taken from box 1 in the right image in B; arrow indicates the point in time of α-actinin removal from the edge, which coincides with dissipation of the protrusion–retraction cycles. Bottom, kymograph taken from box 2 (rotated 90° to the left) in the right image in B. (D) Left, TIRF image of a GFP-α-actinin–expressing cell after 20 min spreading on FN-coated glass (10 µg/ml). Middle, kymograph obtained from the video associated with the image on the left. Right, zoom from the red square highlighted in the middle image. The distribution of α-actinin attains its largest width perpendicular to the leading edge during the onset of the retraction phase.

contraction phase of protrusion–retraction cycles (Giannone *et al.*, 2007). Indeed, the two distinct peaks corresponded with the onset of the retraction phase (Figure 2D) and therefore with maximal force generation on the pillars (Figure 2A).

The two peaks in α-actinin distribution were separated on average by 2 µm (Figure 3, A and B), defining a separation length, L_α, between α-actinin–rich regions. This distance was almost identical to the characteristic length of the local contractions, $L_c = 2.1$ µm (Figure 3C), defined as the separation between the two pillars for which the components of inward and outward deflections along the row axis were maximal. The same value of L_α was found when the cells were plated on pillars (Figure 3D). Also, immunostaining for active myosin molecules (phosphorylated myosin light chain [p-MLC]) showed that they typically localized between α-actinin intensity peaks and between pillars at the cell edge (Figure 3, B and D), consistent with our previous findings (Wolfenson *et al.*, 2016). Control experiments on glass substrates with FN printed dots of the same size and pattern as the pillars (Supplemental Figure S4) showed a similar distribution of both p-MLC and α-actinin. This ruled out possible optical effects due to the PDMS–water interface around the pillars and possible three-dimensional effects of the pillars. Thus the localization pattern of α-actinin corresponded with the contractions of the cell edge.

α-Actinin controls rigidity sensing and links to the general actin flow

Further confirmation that α-actinin was correlated with force application came from experiments using live superresolution imaging (3B microscopy; Cox *et al.*, 2012). In these experiments, we tracked the recruitment of α-actinin to the pillars with high accuracy in parallel to tracking the movements of the pillars with bright-field microscopy (Figure 4A). We obtained sequential superresolution and bright-field images separated by 2.5 s. This sequence showed that α-actinin assembly at the inside half of the pillar immediately preceded the peak inward displacement (Figure 4A and Supplemental Video S6). Further, when we took longer (standard-resolution) videos, we observed that, after the initial recruitment to the pillars, α-actinin was

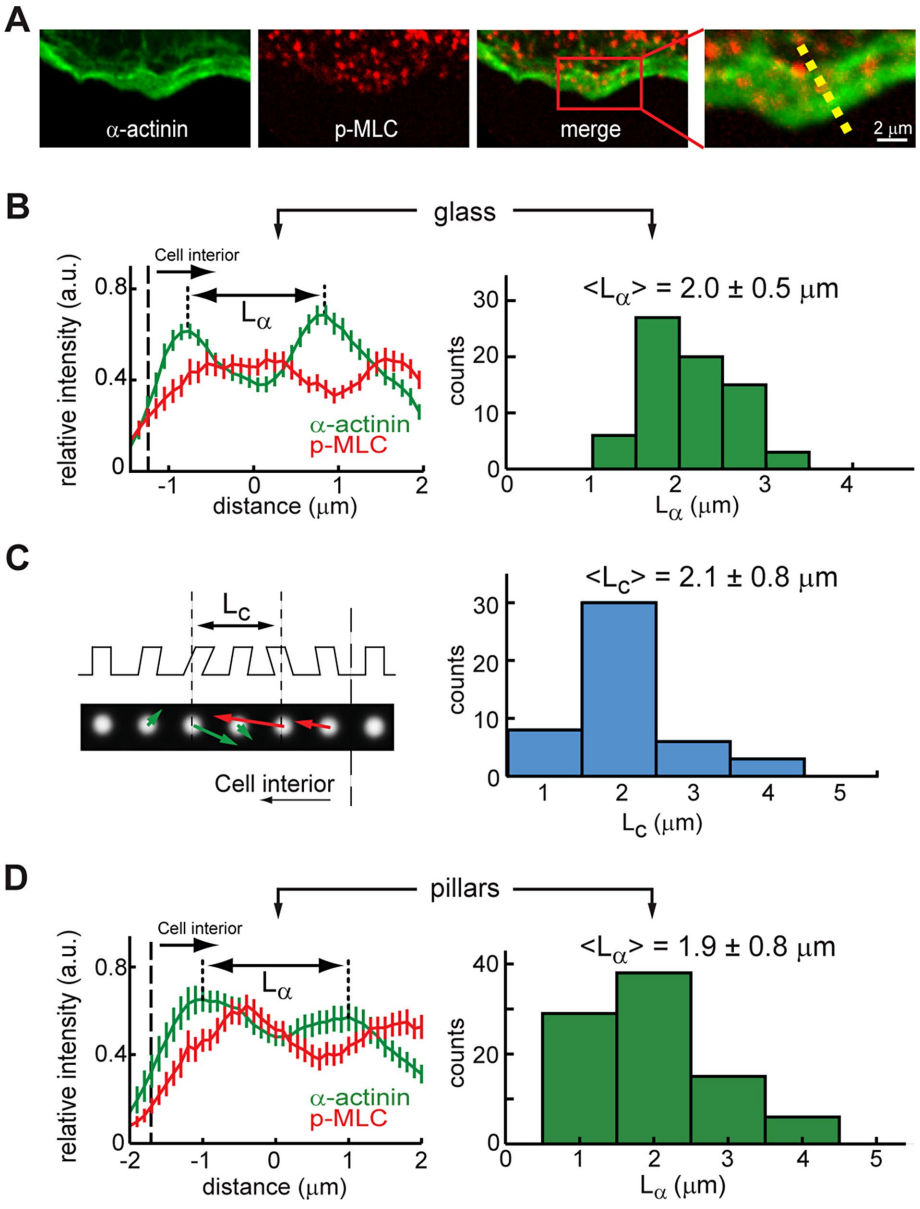

FIGURE 3: Myosin II and α-actinin form contractile units. (A) Fluorescence images of GFP-α-actinin and Alexa Fluor 555 anti p-MLC of a cell spread for 25 min. (B) Left, average profiles of α-actinin and anti p-MLC obtained from multiple positions along the edges of cells plated on FN-coated glass at regions undergoing retraction (see, e.g., the yellow dashed line in A, right); right, histogram of the α-actinin peak-to-peak distance, L_α, as defined on the left (6 cells, $n = 71$ profiles). (C) Left, the contractile unit length, L_c, was defined for each row of pillars perpendicular to the leading edge as the separation between the two pillars showing over time the largest product of the components of inward and outward deflections along the row axis. Deflections were filtered in time with a 5-point moving average. Right, histogram of the contractile unit length, L_c ($n = 47$ rows of pillars, 238 pillars, 3 cells). (D) Left, average profiles of α-actinin and anti p-MLC obtained from the average of multiple positions along the edge of multiple cells plated on FN-coated pillars at regions undergoing retraction; right, histogram of the α-actinin peak-to-peak distance, L_α, as defined on the left ($n = 90$ profiles).

being pulled toward the cell center, resulting in an elongated pattern of the fluorescent signal of GFP-α-actinin (Figure 4B and Supplemental Video S7). Importantly, the recruitment to the CUs was rigidity dependent, evidenced by the higher fluorescence levels of GFP-α-actinin on stiffer pillars (before the elongated pattern appeared) when dual-stiffness pillar arrays were used (Supplemental Figure S5A). These results indicated that α-actinin had a significant role in initial force production and adhesion reinforcement by rigidity-sensing CUs, and subsequent linkage to the rearward-flowing actin during the loss of tension by the CUs.

To test this notion directly, we first conducted pillar contraction experiments after knocking down α-actinin expression. In depleted cells, pillar movements were primarily directed inward, and local contractions were not observed (Figure 4C). Additionally, actin and α-actinin localization were severely affected, and depleted cells showed finger-like protrusions instead of an organized lamellipodium (Supplemental Figure S5B). The average maximal value of displacements by α-actinin–depleted cells was 33 ± 8 nm (Figure 4D). Because local contractions were not observed, these displacements likely reflect only the rearward flow component, and therefore this value should be compared with the 12.5 nm value for actin rearward flow in intact cells. Thus, in the absence of α-actinin, the forces exerted by the actin rearward flow on nascent adhesions are ~2.6-fold higher than in intact cells.

If there were a link between force application by CUs and the protrusion–retraction cycles of the cell edge, then the absence of α-actinin should have also altered the periodic cycles. Indeed, α-actinin-KD cells spreading on FN-coated glass did not display regular protrusion–retraction cycles. Instead, extensive ruffling was observed, which was typically manifested by rapid protrusions of the membrane, followed by abrupt, quick, and long retractions of the cell edge, resulting in it returning to approximately the same starting position (Figure 5A). This resembled the behavior of intact cells on soft surfaces (Giannone *et al.*, 2004), suggesting that α-actinin had a significant role in regulating rigidity sensing. Indeed, α-actinin-KD cells could not differentiate between substrates of different rigidities, evidenced by the fact that they spread to the same extent on pillar arrays that differed by 5.5-fold in stiffness, whereas control cells spread to an ~50% larger area on the stiffer pillars (Figure 5B; control experiments on continuous stiff and soft gels showed a similar trend, ruling out the possibility of aberrant topology sensing in the absence of α-actinin; Supplemental Figure S5C). Interestingly, when plated on soft PDMS gels (0.2 kPa) for 3 d, knocked-down α-actinin (α-actinin-KD) cells were able to proliferate and form multicellular colonies, whereas most control cells did not survive, and the remaining cells did not spread or proliferate (Figure 5C).

DISCUSSION

From our results, a model emerges for the dynamic process of rigidity sensing at the cell edge. The use of submicron-diameter pillars

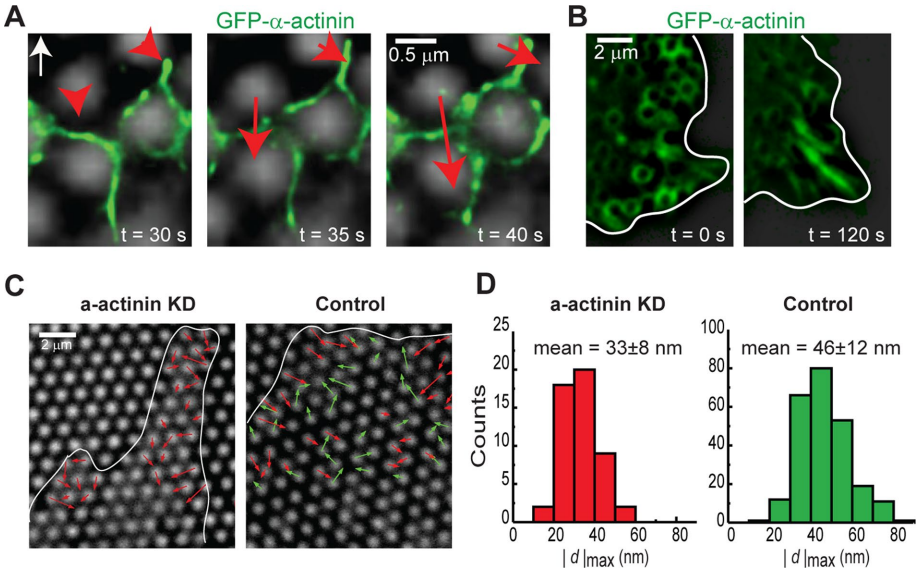

FIGURE 4: α-Actinin's effect on CUs and rigidity sensing. (A) Time-lapse images of a live cell showing the displacement map and GFP-α-actinin localization (3B analysis). α-Actinin concentrates on the inside half of the pillar at the time of peak inward displacement. Displacements are shown only for pillars that were outside the cell at $t = 0$ s and above the noise. The vertical white arrow represents spreading direction. The adhesion complexes initially form around the edges of the pillars, because these are the first points of contact of the cell edge with the matrix when the former is protruding forward. (B) Images taken from Supplemental Video S7 showing initial recruitment of GFP-α-actinin around the pillars, followed by its retraction back toward the cell center, resulting in an elongated pattern. (C) Typical map of pillar deflections under a spreading MEF 20–25 min after plating. Displacements are shown only for pillars that were outside the cell at $t = 0$ s and that had displacements greater than 15 nm for the inward deflection (red arrows) and 20 nm for the outward deflections (green arrows). Left, cells were transfected with α-actinin short hairpin RNA (shRNA). Only inward deflections at the leading edge (red arrows) are observed. Right, cells were transfected with control shRNA. Local contractions involve inward deflections at the leading edge (red arrows) and outward deflections 2–3 μm behind (green arrows). (D) Histograms of maximum displacements, $|d|_{max}$. Differences between α-actinin shRNA cells (left) and control cells (right) were significant (left: $n = 51$ pillars for 4 cells; right: $n = 243$ for 5 cells; $p < 0.001$, Mann-Whitney rank-sum test). Errors are given by the SD (pillar stiffness = 13.9 pN/nm).

allows us to dynamically track forces at the very early stages of adhesion formation, which is not achievable by traction-force microscopy, a commonly used technique for tracking cellular forces (Plotnikov *et al.*, 2012). (See *Materials and Methods* for an explanation of the differences between the two techniques.) The first step after initial contact of the cell edge with new matrix is the formation of sarcomere-like CUs that apply local forces to the matrix. The CUs generate contractile forces on neighboring pillars (adhesions) that are powered by myosin II localized to the regions where contractility is greatest. The CUs have a length of ~2 μm, estimated from the pillar-displacement analysis, that matches the distance between peaks in the α-actinin distribution in the same region in both pillar and flat surfaces (Figure 3). Dynamic measurements of α-actinin recruitment show that its association with pillars correlates with early force generation, and in its absence, cells cannot produce proper contractile forces by CUs (Figure 4). The presence of α-actinin is also important for the appearance of the periodic edge retractions, which are typically observed in control cells on hard surfaces. On knockdown of α-actinin, cells behave on glass as if they were on soft surfaces, showing ruffling at their edges and remaining round and small over time (Figure 4).

To produce displacements, CUs need to contain actin filaments organized into antiparallel arrays (Reymann *et al.*, 2012). This can be realized if filaments originate from early adhesions in multiple directions, as was observed (Yu *et al.*, 2011). These filaments could then bind to integrins through α-actinin, transmitting forces to the ECM, as was recently shown (Roca-Cusachs *et al.*, 2013). Thus α-actinin would be an essential element in CUs, both cross-linking actin and binding actin to integrins. This can explain why α-actinin is required for local contractions and why it is preferentially recruited to pillars, which are points of cell–ECM attachment through integrins. In contrast, α-actinin is not required for substrate deformations mediated by rearward flow. Inward deformations are still present in α-actinin–depleted cells (31 nm mean displacement) and are even larger than the estimated rearward-flow contribution in control cells (~12.5 nm). The reason for this is unclear but may be linked to the competition between α-actinin and talin for binding to integrins at early times (Roca-Cusachs *et al.*, 2013).

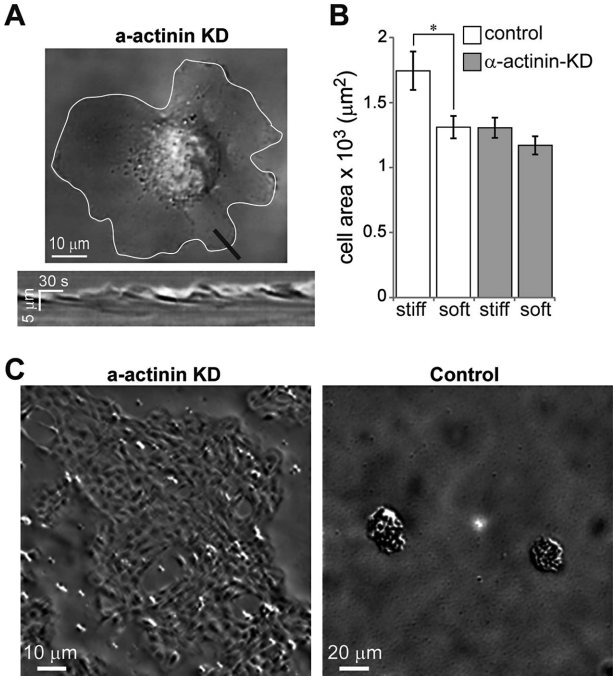

FIGURE 5: α-Actinin depletion affects rigidity sensing. (A) Top, image taken from a video of an α-actinin-KD cell spreading on FN-coated glass; bottom, kymograph from the black line in the top image showing periodic instances of cell-edge protrusions followed by complete retraction to approximately the starting positions. (B) Average area of cells transfected with control and α-actinin shRNA after 1 h of spreading on stiff and soft pillars ($n > 30$ in all cases). *, $p < 0.01$, Student's t test. (C) DIC images of control and α-actinin KD cells after 3 d in culture on 0.2 kPa gels.

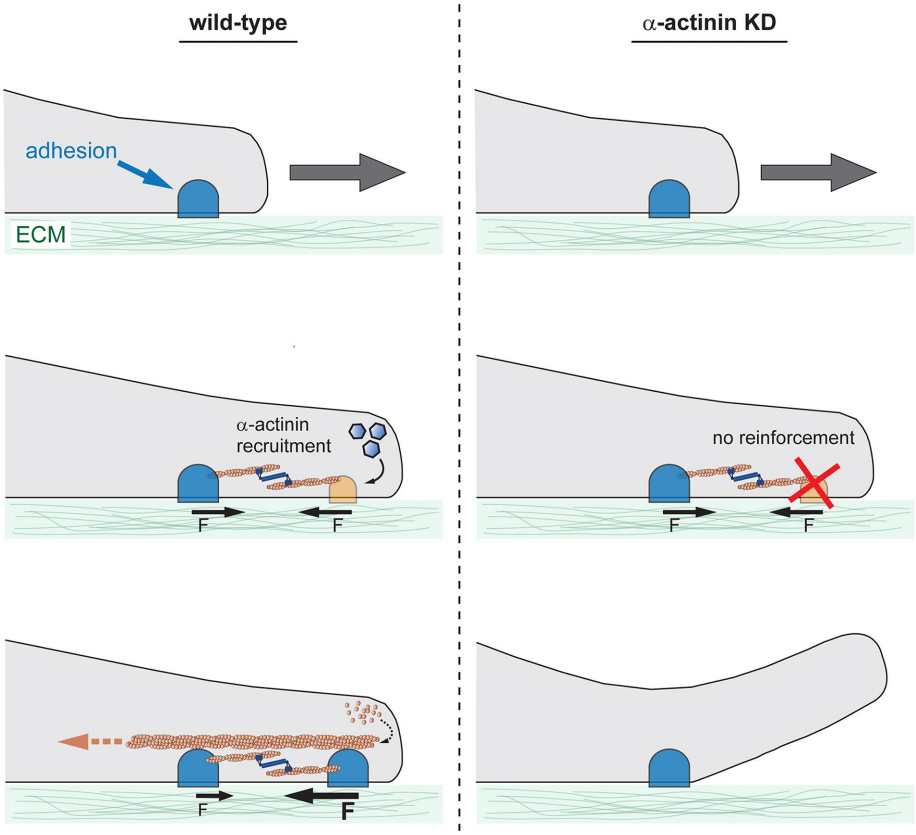

FIGURE 6: Model for α-actinin's role in rigidity sensing. Left, rigidity sensing in the presence of α-actinin. When the cell edge protrudes forward (top), it forms new contact with the matrix (orange dome in middle panel); this triggers the formation of CUs that apply contractile forces on neighboring adhesions, which requires the recruitment of α-actinin to reinforce adhesions (typical distance between the adhesions within a CU is ~2 μm). Subsequently the lamellipodial network (actin flow) applies pulling centripetal forces on the adhesions (bottom). Right, aberrant rigidity sensing in the absence of α-actinin. When the initial contractions occur, and no α-actinin is present to reinforce the adhesions (middle), they eventually break (bottom), resulting in ruffling of the cell edge. Ruffling also occurs in wild-type cells on soft matrices when α-actinin–mediated adhesion reinforcement does not occur and adhesions break (Wolfenson *et al.*, 2016).

Thus the process of rigidity sensing involves a series of steps that all must be successful before the cell can proceed with the next one (Figure 6). One of the critical steps identified recently is the requirement of the CUs to reach a certain force level that activates adhesion reinforcement by recruitment of α-actinin (Wolfenson *et al.*, 2016). The next step is the linkage of these adhesions to the general flow of actin rearward. Importantly, the relative contributions of forces produced by the CUs and by the rearward actin flow depend on matrix rigidity (Figure 1). If the matrix is stiff enough, the resistance to the CU-generated forces is high, which triggers adhesion reinforcement. Consequently, when the adhesions experience actin flow–generated forces (which are constant regardless of rigidity), the linkages are strong enough and they do not break. These strong adhesions then provide support for subsequent cell-edge protrusion (Figure 6). This is the basis for the periodicity of the protrusion–retraction cycles observed in spreading and migrating cells on stiff matrices (Giannone *et al.*, 2004, 2007; Dobereiner *et al.*, 2006; Gupton and Waterman-Storer, 2006). In the absence of α-actinin, reinforcement does not occur, even on stiff surfaces, and the adhesions remain weak and cannot sustain the actin-flow forces. Hence, instead of regular protrusion–retraction cycles, general ruffling of the cell edge is observed (Figure 6). Similarly, when wild-type cells are plated on soft matrices and the contraction does not generate a force greater than the threshold needed to activate adhesion reinforcement, the adhesions break, and ruffling is observed (Wolfenson *et al.*, 2016).

What is unclear is how the high forces produced in the absence of α-actinin allow the cells to proliferate on soft matrices. One possible hypothesis that needs to be tested is that high forces are generated to activate the signaling cascades that promote cell growth. In wild-type cells on rigid surfaces, high forces are normally generated, but in α-actinin-KD cells, such high forces are also generated on soft substrates. This provides a novel view of the mechanosensitivity of cells and may offer a link between rigidity sensing and anchorage-dependent growth of mesenchymal and epithelial cells (Wolfenson *et al.*, 2016).

MATERIALS AND METHODS

Cells culture, constructs, and reagents

MEF cells were cultured at 37°C and 5% CO_2 in DMEM supplemented with 10% fetal bovine serum, 100 IU/ml penicillin–streptomycin, 2 μM L-glutamine, and 2 μM HEPES. One day before the experiments, cells were sparsely plated to minimize cell–cell interactions before replating during the experiments. Transfection of GFP-α-actinin (Roca-Cusachs *et al.*, 2013) was carried out using the Amaxa Nucleofector System (Lonza, Allendale, NJ), with 10^6 cells per reaction and 5–6 μg DNA. Cells were transfected 1–2 d before measurements. For immunofluorescence microscopy, cells were fixed with 4% paraformaldehyde, permeabilized with 0.1% Triton X-100, and labeled with polyclonal rabbit antibodies against phospho-myosin light chain 2 (1 h at room temperature [RT]; Cell Signaling; Thr-18/Ser-19) and then Alexa Fluor 555–conjugated immunoglobulin G secondary antibodies (1 h, RT; Invitrogen, Carlsbad, CA). α-Actinin knockdown was carried out as described previously (Roca-Cusachs *et al.*, 2013). The 0.2 kPa PDMS gels used for testing α-actinin-KD cells' growth on soft matrices were purchased from Soft Substrates (San Diego, CA).

Pillar fabrication, video microscopy, and pillar-displacement measurements

Pillars provide an excellent tool for measuring forces in nascent adhesions, since each pillar constitutes a single localized point of force application. In contrast, in the continuous gels used in traction-force microscopy (e.g., in Plotnikov *et al.*, 2012), force is applied at multiple points (early adhesions) and would displace beads in the gel all around those points in different directions. Thus the force measurement is averaged out over the area around each of the adhesions before mature focal adhesions are formed. Moreover, such areas are without clear and defined borders. Instead, traction-force microscopy is good for obtaining maps of the stress that cells apply to the substrate.

Fabrication of pillar arrays with diameters of 500 nm was carried out as previously reported (Ghassemi *et al.*, 2012). Molds for fabrication of pillar arrays with two rigidities, that is, with diameters of 400 and 750 nm, were fabricated using electron-beam lithography in hard poly(methyl methacrylate) (PMMA) substrates. PMMA was first spin-coated onto a silicon substrate and then hard-baked on a hot plate for 10 h. An electron-beam lithography tool (NanoBeam nB5; NanoBeam, Cambridge, UK) was then used to pattern holes in the PMMA. The depth of holes was dependent on the thickness of the PMMA. Pillar-bending stiffness, k, was calculated from the linear elastic theory of a cylinder of diameter, D, and length, H, bent by the application of a lateral force at its extremity: $= \frac{3}{64}\pi E\frac{D^4}{H^a}$, where E is the Young's modulus of the material (2 mPa for the PDMS we used). The 750-nm-diameter pillars were thus ~12-fold stiffer than the 400 nm pillars. Importantly, both diameters were small enough so that contractile units would form between pillars and not span single pillars (see Ghassemi *et al.*, 2012).

In all cases, the center-to-center spacing between pillars was twice the pillar diameter.

Pillar-displacement measurements were performed on pillar arrays coated with 10 μg/ml of FN (Invitrogen), as previously described. Image software to generate displacement maps was written in Matlab (MathWorks, Natick, MA) and used as input for the coordinates of pillar centers determined with the ImageJ (National Institutes of Health, Bethesda, MD) plug-in Nano Tracking, which uses an autocorrelation algorithm (Gelles *et al.*, 1988). For removal of stage drift, the average displacement of a set of pillars far from any cells was subtracted from the data. Finally, the position versus time data for each pillar were low-pass filtered with a cutoff frequency of 0.15 Hz.

For cell-spreading experiments on pillars, the cells were trypsinized, washed with soybean trypsin inhibitor, centrifuged, and preincubated in Ringer's medium (150 mM NaCl, 5 mM KCl, 1 mM $CaCl_2$, 1 mM, $MgCl_2$, 20 mM HEPES and 2 g/l D-glucose at pH 7.4) for 30 min before the experiment. Time-lapse imaging of the pillars was performed with bright-field microscopy using a CoolSNAP HQ (Photometrics, Tucson, AZ) attached to an inverted microscope (Olympus IX-70; Olympus America, Center Valley, PA) maintained at 37°C. Images were mostly recorded at 1 or 0.5 Hz using a 100× or 60×, 1.4 NA, oil-immersion Olympus objective. For establishment of a reference of zero force, only pillars that were initially outside the cell were analyzed, with the exception of Figure 1B, where pillar displacements in the nuclear region are also shown. In the latter case, each arrow in the nuclear region represents a pillar-displacement vector that differs from the real displacement by an unknown vector (since initial rest position was not known).

Statistical and error analysis

The noise of the system was measured by tracking pillars not associated with any cells. For both directions, inward and outward, we determined the upper limit for the apparent pillar displacement caused by optical distortions upon cell–pillar contact (lensing effect) by tracking the positions of ultrastiff pillars (k = 680 pN/nm) as a cell moved over them. Maximum outward was 9 ± 4 nm (mean ± SD), similar to the noise value found for flexible pillars, and maximum inward was –17 ± 4 nm (mean ± SD). For all of the pillars used in this work, the distributions of maximum displacements for both directions were clearly distinct from the distributions on ultrastiff pillars, with negligible p values (< 0.0001). We also studied the dynamics of displacements. On ultrastiff pillars, the displacement direction changed faster than on flexible pillars and was outward initially. In conclusion, the observed contractions of flexible pillars were not due to optical artifacts.

Statistical comparisons were done with two-tailed Student's t tests when two cases were compared and with analysis of variance tests for multiple comparisons. When data did not meet the normality criteria, Mann-Whitney rank-sum tests were performed instead.

Fluorescence profiles in Figure 3: for every pillar row the fluorescence profile (averaged over its 0.5 μm width) of both α-actinin-GFP and anti-pMLC was taken. Intensity traces were aligned so as to have the middle point between two α-actinin peaks corresponding to the coordinate x = 0 μm. Then each profile was subtracted from the background and normalized by its maximum value. Finally, for each spatial interval of 100 nm the average and the SE were taken over all profiles. The error bars represent the SE (2 cells, 22 profiles, >10 profiles for each cell). The vertical dashed line represents the approximate cell edge position.

Fluorescence and DIC microscopy

TIRF and DIC time-lapse micrographs of GFP-α-actinin were taken (at 6.7 Hz for TIRF and at 1 Hz for DIC) using an Olympus IX81 fluorescence microscope maintained at 37°C with a 60× (and 100× for DIC), 1.45 NA, oil-immersion Olympus objective, an electron-multiplied CCD camera (model Cascade-II:512, Photometrics), and a further 1.6× magnification of 5.95 pixels/μm. Immunofluorescence sample images were taken with a Zeiss LSM 700 laser-scanning confocal microscope, using 63×, 1.4 NA, oil-immersion objective. Cover glasses were washed for 2 h in 20% nitric acid, silanized by exposure to gaseous 1, 1, 1, 3, 3, 3-hexamethyldisilazane (Sigma), and coated with 600 ml of a 10 μg/ml human plasma full-length pure FN (Roche) solution for 1 h at 37°C.

Imaging for 3B analysis

For live-cell imaging of the pillars and GFP-α-actinin, a series of 100 images was taken at 50 Hz in the GFP channel (2 s), followed by a single bright-field image (~3 s to switch the channel and acquire the image); this sequence was repeated 18 times. The 3B analysis was done as described in Cox *et al.* (2012). Because of the computational cost, the 3B software was run on a Titan cluster (http://wiki.c2b2.columbia.edu/systems/index.php/Documentation/Titan_cluster) at the Center for Computational Biology and Bioinformatics (Columbia University, New York).

Printed surfaces

Printed surfaces were prepared as previously described (Kung *et al.*, 2000; Schmid and Michel, 2000; Shen *et al.*, 2008). Glass coverslips were cleaned by immersion in hot detergent (Linbro 7×, diluted 1:3 with deionized water), rinsed with MilliQ-grade water, and then baked at 450°C for 6 h. For microcontact printing, hPDMS was prepared in the following way: 3.4 g of VDT-731 (Gelest) were mixed with 1 g of HMS-301 in 50 ml tube, and 4 droplets of modulator were added and mixed. The silicon wafer–molding surface was covered thoroughly with thin layer of hPDMS and baked at 60°C for 20–40 min. Regular PDMS was used to make a composite stamp with the hPDMS as a printing surface and then coated with FN-A568 that was printed on the glass coverslips.

Immunofluorescence sample images

Images in Supplemental Figure 4 were taken with a Zeiss LSM 700 laser scanning confocal microscope, using 63×/1.4 NA, oil immersion, Zeiss objective; an Olympus Fluoview FV500 laser-scanning confocal microscope, using 60×/1.4 NA, oil immersion, Olympus objective; and a 100× objective in a Leica SP5 laser-scanning confocal microscope.

ACKNOWLEDGMENTS

We thank Nicolas Biais for experimental support, reading the paper, and comments; Edward Rosten and Susan Cox for technical support with the 3B software; Xian Zhang for providing the raw data for the 3B analysis control; Virginie Stévenin for assistance with the figures; Luis Carlos Santos for experimental support; and all the members of the Sheetz lab for their support. This work was funded by the National Institutes of Health (NIH) Common Fund Nanomedicine program (PN2 EY016586) and the NIH grant "Analysis of 120 nm local contractions linked to rigidity sensing" (1 R01 GM100282-01). The fabrication work was performed at the Cornell NanoScale Facility, a member of the National Nanotechnology Infrastructure Network, which is supported by National Science Foundation Grant ECS-0335765. H.W. was supported by a Marie Curie International Outgoing Fellowship within the Seventh European Commission Framework Programme (PIOF-GA-2012-332045). T.I. was supported by a postdoctoral fellowship from the American Heart Association. M.P.S was partially supported by the Mechanobiology Institute, National University of Singapore.

REFERENCES

Chan CE, Odde DJ (2008). Traction dynamics of filopodia on compliant substrates. Science 322, 1687–1691.

Chen L, Vicente-Manzanares M, Potvin-Trottier L, Wiseman PW, Horwitz AR (2012). The integrin-ligand interaction regulates adhesion and migration through a molecular clutch. PLoS One 7, e40202.

Choi CK, Vicente-Manzanares M, Zareno J, Whitmore LA, Mogilner A, Horwitz AR (2008). Actin and alpha-actinin orchestrate the assembly and maturation of nascent adhesions in a myosin II motor-independent manner. Nat Cell Biol 10, 1039–1050.

Cox S, Rosten E, Monypenny J, Jovanovic-Talisman T, Burnette DT, Lippincott-Schwartz J, Jones GE, Heintzmann R (2012). Bayesian localization microscopy reveals nanoscale podosome dynamics. Nat Methods 9, 195–200.

Dobereiner HG, Dubin-Thaler B, Giannone G, Xenias HS, Sheetz MP (2004). Dynamic phase transitions in cell spreading. Phys Rev Lett 93, 108105.

Dobereiner HG, Dubin-Thaler BJ, Hofman JM, Xenias HS, Sims TN, Giannone G, Dustin ML, Wiggins CH, Sheetz MP (2006). Lateral membrane waves constitute a universal dynamic pattern of motile cells. Phys Rev Lett 97, 038102.

Dubin-Thaler BJ, Hofman JM, Cai Y, Xenias H, Spielman I, Shneidman AV, David LA, Dobereiner HG, Wiggins CH, Sheetz MP (2008). Quantification of cell edge velocities and traction forces reveals distinct motility modules during cell spreading. PLoS One 3, e3735.

Elosegui-Artola A, Bazellieres E, Allen MD, Andreu I, Oria R, Sunyer R, Gomm JJ, Marshall JF, Jones JL, Trepat X, *et al.* (2014). Rigidity sensing and adaptation through regulation of integrin types. Nat Mater 13, 631–637.

Gauthier NC, Fardin MA, Roca-Cusachs P, Sheetz MP (2011). Temporary increase in plasma membrane tension coordinates the activation of exocytosis and contraction during cell spreading. Proc Natl Acad Sci USA 108, 14467–14472.

Gelles J, Schnapp BJ, Sheetz MP (1988). Tracking kinesin-driven movements with nanometre-scale precision. Nature 331, 450–453.

Ghassemi S, Meacci G, Liu S, Gondarenko AA, Mathur A, Roca-Cusachs P, Sheetz MP, Hone J (2012). Cells test substrate rigidity by local contractions on submicrometer pillars. Proc Natl Acad Sci USA 109, 5328–5333.

Giannone G, Dubin-Thaler BJ, Dobereiner HG, Kieffer N, Bresnick AR, Sheetz MP (2004). Periodic lamellipodial contractions correlate with rearward actin waves. Cell 116, 431–443.

Giannone G, Dubin-Thaler BJ, Rossier O, Cai Y, Chaga O, Jiang G, Beaver W, Dobereiner HG, Freund Y, Borisy G, *et al.* (2007). Lamellipodial actin mechanically links myosin activity with adhesion-site formation. Cell 128, 561–575.

Gupton S, Waterman-Storer C (2006). Spatiotemporal feedback between actomyosin and focal-adhesion systems optimizes rapid cell migration. Cell 125, 1361–1374.

Humphrey JD, Dufresne ER, Schwartz MA (2014). Mechanotransduction and extracellular matrix homeostasis. Nat Rev Mol Cell Biol 15, 802–812.

Iskratsch T, Wolfenson H, Sheetz MP (2014). Appreciating force and shape—the rise of mechanotransduction in cell biology. Nat Rev Mol Cell Biol 15, 825–833.

Kung LA, Kam L, Hovis JS, Boxer SG (2000). Patterning hybrid surfaces of proteins and supported lipid bilayers. Langmuir 16, 6773–6776.

Ladoux B, Nicolas A (2012). Physically based principles of cell adhesion mechanosensitivity in tissues. Reports on progress in physics. Phys Soc 75, 116601.

Lu P, Weaver VM, Werb Z (2012). The extracellular matrix: a dynamic niche in cancer progression. J Cell Biol 196, 395–406.

Machacek M, Hodgson L, Welch C, Elliott H, Pertz O, Nalbant P, Abell A, Johnson GL, Hahn KM, Danuser G (2009). Coordination of Rho GTPase activities during cell protrusion. Nature 461, 99–103.

Parsons JT, Horwitz AR, Schwartz MA (2010). Cell adhesion: integrating cytoskeletal dynamics and cellular tension. Nat Rev Mol Cell Biol 11, 633–643.

Petrie RJ, Doyle AD, Yamada KM (2009). Random versus directionally persistent cell migration. Nat Rev Mol Cell Biol 10, 538–549.

Plotnikov SV, Pasapera AM, Sabass B, Waterman CM (2012). Force fluctuations within focal adhesions mediate ECM-rigidity sensing to guide directed cell migration. Cell 151, 1513–1527.

Reymann AC, Boujemaa-Paterski R, Martiel JL, Guerin C, Cao W, Chin HF, De La Cruz EM, Thery M, Blanchoin L (2012). Actin network architecture can determine myosin motor activity. Science 336, 1310–1314.

Roca-Cusachs P, del Rio A, Puklin-Faucher E, Gauthier NC, Biais N, Sheetz MP (2013). Integrin-dependent force transmission to the extracellular matrix by alpha-actinin triggers adhesion maturation. Proc Natl Acad Sci USA 110, E1361–E1370.

Ryan GL, Watanabe N, Vavylonis D (2012). A review of models of fluctuating protrusion and retraction patterns at the leading edge of motile cells. Cytoskeleton 69, 195–206.

Schmid H, Michel B (2000). Siloxane polymers for high-resolution, high-accuracy soft lithography. Macromolecules 33, 3042–3049.

Shen K, Thomas VK, Dustin ML, Kam LC (2008). Micropatterning of costimulatory ligands enhances CD4+ T cell function. Proc Natl Acad Sci USA 105, 7791–7796.

Watt FM, Huck WT (2013). Role of the extracellular matrix in regulating stem cell fate. Nat Rev Mol Cell Biol 14, 467–473.

Wolfenson H, Lavelin I, Geiger B (2013). Dynamic regulation of the structure and functions of integrin adhesions. Dev Cell 24, 447–458.

Wolfenson H, Meacci G, Liu S, Stachowiak MR, Iskratsch T, Ghassemi S, Roca-Cusachs P, O'Shaughnessy B, Hone J, Sheetz MP (2016). Tropomyosin controls sarcomere-like contractions for rigidity sensing and suppressing growth on soft matrices. Nat Cell Biol 18, 33–42.

Xu K, Babcock HP, Zhuang X (2012). Dual-objective STORM reveals three-dimensional filament organization in the actin cytoskeleton. Nat Methods 9, 185–188.

Yu CH, Law JB, Suryana M, Low HY, Sheetz MP (2011). Early integrin binding to Arg-Gly-Asp peptide activates actin polymerization and contractile movement that stimulates outward translocation. Proc Natl Acad Sci USA 108, 20585–20590.